The effect of unsteady and baroclinic forcing on predicted wind profiles in Large Eddy Simulations: Two case studies of the daytime atmospheric boundary layer

Pedersen, Jesper Grønnegaard; Kelly, Mark C.; Gryning, Sven-Erik; Brümmer, Burghard

Published in:
Meteorologische Zeitschrift

Link to article, DOI:
10.1127/0941-2948/2013/0477

Publication date:
2013

Document Version
Publisher's PDF, also known as Version of record

Meteorologische Zeitschrift, Vol. 22, No. 6, 661–674 (published online October 2013)

Open Access Article

The effect of unsteady and baroclinic forcing on predicted wind profiles in Large Eddy Simulations: Two case studies of the daytime atmospheric boundary layer

JESPER GRØNNEGAARD PEDERSEN[1,*], MARK KELLY[1], SVEN-ERIK GRYNING[1] and BURGHARD BRÜMMER[2]

[1]DTU Wind Energy, Risø Campus, Technical University of Denmark, 4000 Roskilde, Denmark
[2]Meteorological Institute, University of Hamburg, Germany

(Manuscript received March 3, 2013; in revised form June 9, 2013; accepted June 10, 2013)

Abstract

Due to its fine-resolution requirement and subsequent computational demand, Large Eddy Simulation of the atmospheric boundary layer is limited in most cases to computational domains extending only a few kilometers in both the vertical and horizontal directions. Variations in the flow and in relevant atmospheric fields (e.g. temperature) that occur at larger scales must be imposed through boundary conditions or as external forcing. In this work we study the influence of such variations on the wind profile in Large Eddy Simulations of daytime atmospheric boundary layers, by comparing observations with simulations that use progressively more realistic forcing relative to observed large-scale pressure gradients.

Two case studies are presented. One is based on measurements from the rural site of Høvsøre in Denmark, and the other on measurements from a suburban site in Hamburg, Germany. The applied domain-scale pressure gradient and its height- and time-dependence are estimated from LIDAR measurements of the wind speed above the atmospheric boundary layer in the Høvsøre case, and from radio soundings and a network of ground-based pressure sensors in the Hamburg case.

In the two case studies, LIDAR measurements of the wind speed up to heights between 900 and 1600 m and tower-based measurements up to 100 and 250 m are used to evaluate the performance of the variably-driven Large Eddy Simulations. We find in both case studies that including height- and time-variations in the applied pressure gradient has a significant influence on simulated wind speeds, and improves agreement with measured wind speeds, especially in the Høvsøre case. In the Hamburg case, an overly simplified specification of the height dependence of the forcing, as well as the influence of phenomena such as large-scale subsidence and advection, tend to reduce agreement with measurements, relative to the Høvsøre case. The Hamburg case illustrates that measurements of the surface pressure gradient and relatively infrequent radio soundings alone are not sufficient for accurate estimation of a height- and time-dependent pressure gradient.

Keywords: Large Eddy Simulation, mesoscale phenomena, baroclinity, Wind LIDAR, Wind profile.

1 Introduction

Since the method was introduced with the work of DEARDORFF (1970) and DEARDORFF (1972), Large Eddy Simulation (LES) has become a widely used tool for studying the turbulent flow of the atmospheric boundary layer (ABL). While the general increase in available computer power over the last four decades has made way for simulations of yet finer resolution, the size of the computational domain used in most LES studies has not changed as much. A domain twice as high as the ABL with horizontal dimensions two or three times the vertical extent is often assumed to be sufficiently large, to accommodate most flow structures expected to develop during the simulation time. Thus the size of a typical high-resolution atmospheric LES domain is on the order of $400 \times 400 \times 400$ m^3 (BEARE et al., 2006) for cases with stable stratification and $5 \times 5 \times 2$ km^3 (SULLIVAN and PATTON, 2011) for convective conditions.

It is, however, also well known that the atmosphere contains motions of air varying over spatial and temporal scales larger than a few kilometers and hours, i.e. meso- and synoptic-scale phenomena. Due to the high computational expense, it is generally not feasible to perform high-accuracy LES covering these motions; consequently, if they are to be included in an LES, they must be imposed through boundary conditions or as external forcing. The purpose of this paper is to investigate how simulated wind speeds are affected by application of pressure gradients having time- and height-variations estimated from multiple measurements: LIDAR observations of the wind speed above the ABL, as well as radio

*Corresponding author: Jesper Grønnegaard Pedersen, DTU Wind Energy, Risø Campus, Technical University of Denmark, 4000 Roskilde, Denmark, e-mail: jegp@dtu.dk

DOI 10.1127/0941-2948/2013/0477
0941-2948/2013/0477 $ 6.30

soundings and a network of ground-based pressure sensors.

In the case of a balance between a pressure gradient driving the wind and the Coriolis force due to the rotation of the Earth, the wind is geostrophic and directly proportional to the pressure gradient. Such a balance can only exist above the ABL where the flow is non-turbulent and decoupled from surface influences. Even there, however, it is often disturbed by e.g. movements of synoptic high and low pressure systems and phenomena such as sea breezes with associated temporal variations in the pressure field. Exact geostrophic balance furthermore requires equispaced, parallel and straight isobars (ARYA, 2001). Thus, even above the ABL the observed wind is rarely geostrophic and care has to be taken when relating it to the driving pressure gradient. In addition, variation with height of the pressure gradient caused by large scale horizontal temperature gradients – also known as baroclinity – is often observed and affects the wind profile, as modeled by e.g. ZILITINKEVICH and ESAU (2005); GRYNING et al. (2007); KELLY and GRYNING (2010).

In many applications of LES it is, however, adequate and even desirable to use idealized assumptions regarding the pressure gradient driving the mean flow. For instance, prescribing a forcing which is constant with both time and height provides an attractive framework for research of specific ABL phenomena with a minimum of complications (e.g. SCHMIDT and SCHUMANN, 1989; MOENG and SULLIVAN, 1994; SULLIVAN et al., 1998; KOSOVIC and CURRY, 2000; BEARE et al., 2006).

On the other hand, if the ambition is to use an LES to simulate a realistic atmospheric flow for e.g. prediction of wind speed or model validation through comparison of simulated wind speeds with atmospheric measurements, then appropriately modelled variations in the driving force are necessary. DEARDORFF (1974) used a height-dependent pressure gradient roughly estimated from observational data from day 33 of the Wangara experiment (CLARKE et al., 1971) to force an LES of the unstable ABL, but – despite the applied height dependence – concludes that variations in the forcing must be modeled more accurately to achieve satisfying agreement between simulated and measured wind speeds. BASU et al. (2008) use data from the same experiment in an LES study of the diurnal cycle, with forcing as a function of height applied via parabolic profiles fitted to surface measurements of geostrophic and thermal winds (CLARKE et al., 1971), and temporal variations derived through linear interpolation between measurements. The simulation reproduces prominent features of the observed flow, but significant differences are observed between simulated and measured wind speed and direction, particularly during the afternoon of day 33. BASU et al. (2008) attribute part of the disagreement to inaccuracy in the applied pressure gradient, but the relative importance of this source of error is not clear.

KUMAR et al. (2010) addresses this issue by performing a set of six LESs of two subsequent diurnal cycles with different assumptions for the forcing and surface boundary conditions, based on data from the CASES 99 campaign. Using geostrophic forcings derived from a mesoscale simulation, they show in this case that a simulation with constant pressure gradient gives better agreement with measured wind speed profiles in the surface layer (up to 55 m) than simulations with time- and/or height-dependent forcing. However, when comparing to radio soundings covering the entire ABL, the LES driven with temporally and spatially varying forcing are reported to give the best agreement.

In this paper, we continue along the lines of KUMAR et al. (2010) and compare measured wind speeds to simulated wind speeds from LESs driven by pressure gradients derived from measurements; this includes forcings which are constant, temporally varying, and functions of both time and height. Two case studies are presented. One is based on a set of measurements from the Danish National Test Station for wind turbines at Høvsøre (Denmark), and the other is based on measurements from a site in Hamburg (Germany).

Continuous Doppler LIDAR measurements of the wind speed – covering most of the ABL in the Hamburg case study and the entire ABL and a region above it in the Høvsøre case study – set the two datasets apart from e.g. the Wangara and CASES-99 datasets, and provide an outstanding opportunity for comparison between simulated and measured wind speeds. Tower-based measurements accompany the LIDAR measurements at both sites, and the Hamburg case study furthermore includes radio soundings and measurements of the surface pressure at three locations around the city.

Further details of the two sites and of the measurements are given in section 2. The case studies are described in section 3, and the LES model and the setup of the simulations in section 4. Results are presented and discussed in sections 5 and 6. Section 7 provides a conclusion of our findings.

2 Sites and measurements

Maps of the areas surrounding the Høvsøre and Hamburg sites are shown in Fig. 1.

2.1 The Høvsøre site

The Høvsøre site is located in a rural area approximately 2 km inland from the west coast of Denmark. Sonic and cup anemometers mounted on a meteorological mast at the site (56° 26′ 26.0″ N; 08° 09′ 03.1″ E) provide flux and wind speed measurements at multiple heights from 10 m above ground level up to 116.5 m; for details see FLOORS et al. (2013). Wind vanes provide the wind direction at 10, 60 and 100 m. In addition a Vaisala CL31 ceilometer was operating at the site during the period we study here.

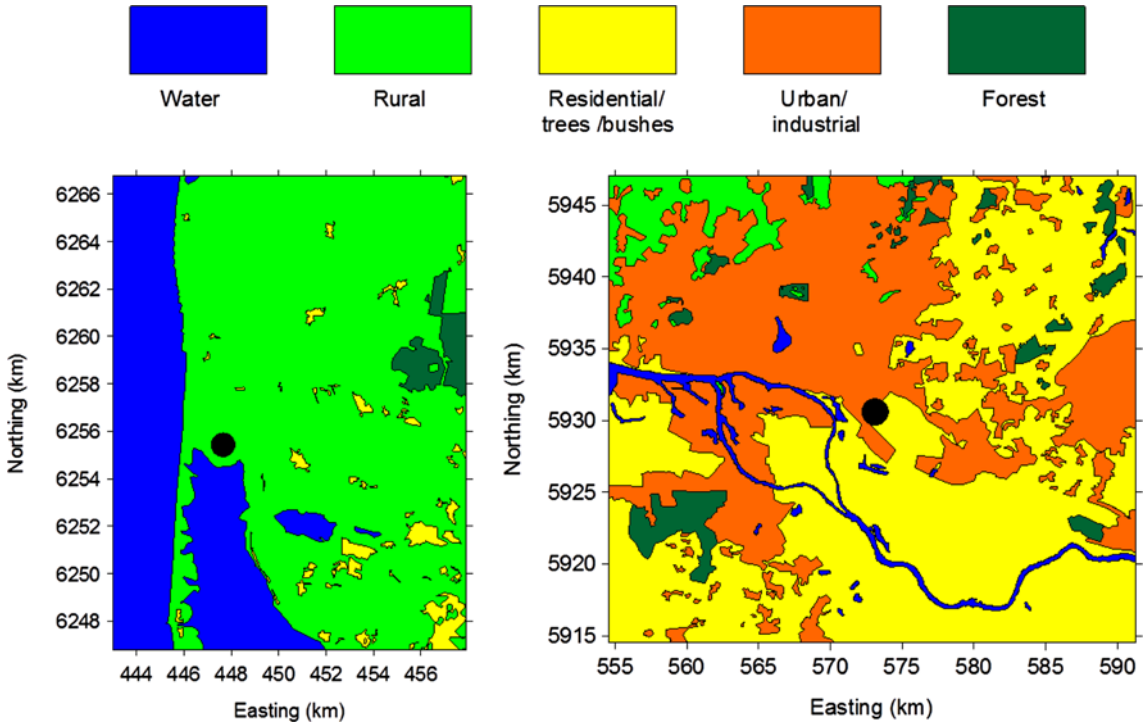

Figure 1: Maps of the areas around the Høvsøre site (left) and the Hamburg site (right). The sites are marked by circles.

2.2 The Hamburg site

The site in Hamburg is located in a suburban area approximately 8 km south-east of the city centre. A 12 m meteorological mast at (53° 31′ 11.7″ N; 10° 06′ 18.5″ E) and a TV tower 170 m to the west-south-west at (53° 31′ 09.0″ N; 10° 06′ 10.3″ E) are instrumented with sonic anemometers at 10 m and at 50, 110, 175, 250 and 280 m respectively (BRÜMMER et al., 2012). These provide measurements of wind speed, wind direction and turbulent fluxes. Sensors measuring the surface pressure are positioned at the site and at two locations 37 km north and 27 km north-west of it. Furthermore, as a supplement to the ground- and tower-based measurements, radiosondes were released from the Hamburg site approximately every two hours between 15 June and 20 June 2011 as part of an intensive measuring campaign. Various ceilometers at the Hamburg site provide estimates of the ABL height.

2.3 Wind LIDAR

A pulsed long-range wind LIDAR (WindCube^{TM} WLS70 by LEOSPHERE) was operating at the Høvsøre site between April 2010 and March 2011 and in Hamburg between April 2011 and April 2012. At both sites it was set up to do conical scans at an angle of 15° to zenith. Measurements of the radial wind speed were performed at four azimuth angles separated by 90° and at heights separated by 50 m. The maximum measuring height of the LIDAR depends on the atmospheric conditions and can be up to 2 km.

Time- and space-averaged values of the horizontal and vertical wind speed components are derived from the measured radial wind speeds. The transmitted pulse length is approximately 200 ns corresponding to a vertical sampling length of 50 m, and a full 360° conical scan takes around 30 s. Due to the conical scanning pattern the horizontal distance over which averages are made increases with height. For a somewhat similar LIDAR system (WindCube^{TM} WLR7 by LEOSPHERE) scanning at angle of 30° to zenith, MIKKELSEN (2009) predicted the relative error on the measured wind speed induced by the spatial averaging to be around 0.5% at a height of 300 m.

3 Case studies

The two case studies presented here are based on data selected from one year of LIDAR measurements at the Høvsøre site and one week of simultaneous LIDAR and radiosonde measurements at the Hamburg site. For the large eddy simulations we use a code developed at the National Center for Atmospheric Research (NCAR) based on assumptions of a dry atmosphere and a horizontally homogeneous flow. Thus, we focus on periods with predominately clear skies and no precipitation. The homogeneity of the flow in the two case studies is discussed in the following subsections. Furthermore, we have sorted the data to find periods with positive heat flux

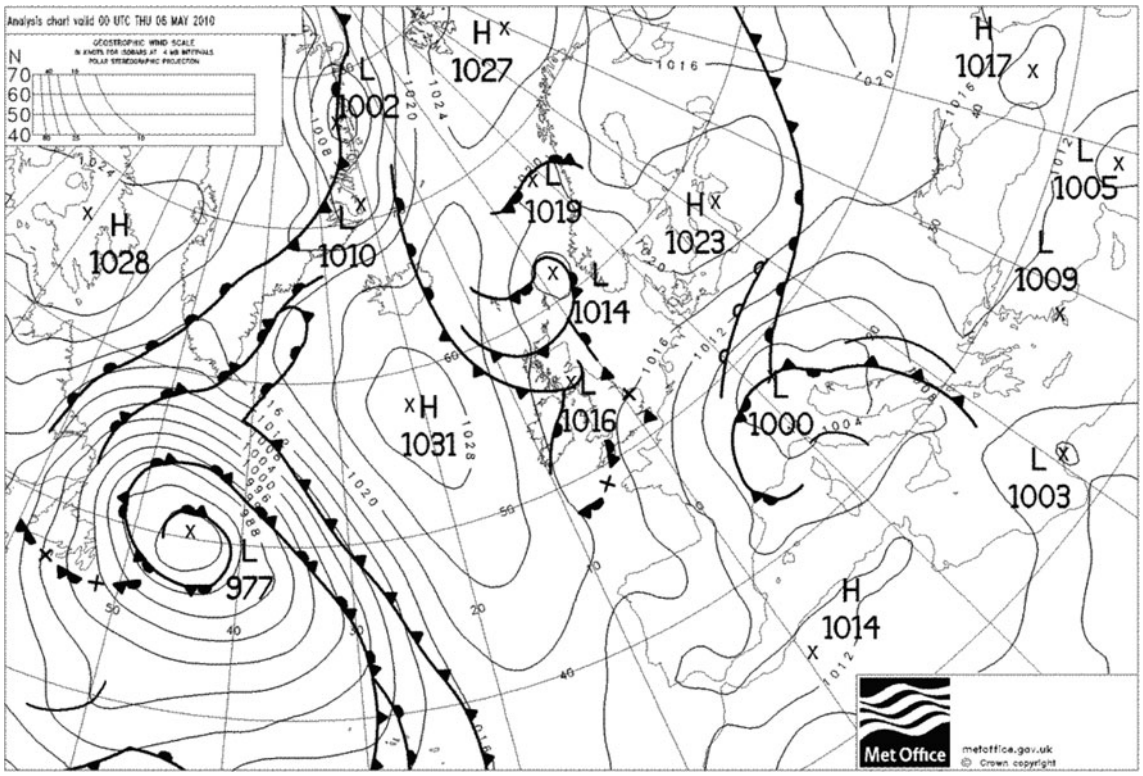

Figure 2: Met Office weather analysis chart valid at 01:00 CET on 6 May 2010 (Høvsøre case study).

near the surface, since convective conditions are typically handled well by LES – even at moderate grid resolution.

3.1 Høvsøre case study

In the Høvsøre case study we focus on the period between 08:00 and 13:00 CET on 6 May 2010. Fig. 2 displays a weather analysis map (courtesy UK Met Office, http://www.wetterzentrale.de/archive/2010/brack/bracka20100506.gif) valid for 01:00 CET, which shows a high pressure system centered above Latvia causing easterly winds across Denmark. This agrees well with the wind direction observed at the site. A warm front located over Central and Eastern Europe is moving towards Denmark, but is presumably too far from Høvsøre to influence the conditions at the site during the period of this case study. By choosing a case with easterly winds, we avoid the influence of the coastline west of the site. The terrain east of the site is flat and covered mainly by grass and various agricultural crops. The flow at the site can to a large extent be assumed to be horizontal homogeneous.

The ABL height estimated from onsite ceilometer measurements increased from 600 m in the morning to 900 m in the afternoon. As the maximum measuring height of the LIDAR during the same period varied between 900 and 1600 m, we have continuous measurements of the wind speed above the ABL from which we estimate the driving pressure gradient. These measurements show a general increase of the mean wind speed during the period studied here (see Fig. 3). Consequently the observed wind above the ABL is not simply geostrophic, and cannot directly be translated into a pressure gradient. However, by approximating the acceleration and assuming that the only forces acting on the wind above the ABL are those arising from the pressure gradient and the rotation of the Earth (i.e. Coriolis force), we are able to estimate the effective pressure gradient and its time dependence. Moreover, a decrease with height of the observed wind speed above the ABL (see Fig. 3) indicates a decrease of the driving pressure gradient, suggesting baroclinic conditions. We use this information to define the domain-scale pressure gradient applied in the LESs of the Høvsøre case described in the following sections. Time series of the measured wind speed at 250 and 750 m are shown in Fig. 4.

3.2 Hamburg case study

In the Hamburg case study we use measurements from the period between 9:00 and 15:30 CET on 15 June 2011. The UK Met Office weather analysis chart from 01:00 CET on this day (Fig. 5, http://www.wetterzentrale.de/archive/2011/brack/bracka20110615.gif) shows several fronts approaching Hamburg from the south-west. The two nearest are warm fronts which might have affected the conditions at the site during the period of this case study. The observed cloud cover does, however, remain sparse during most of the period.

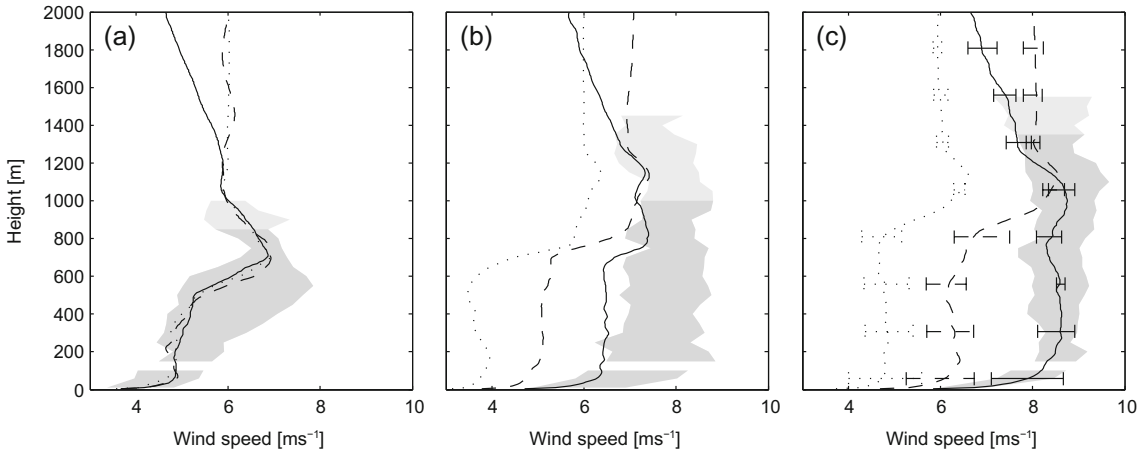

Figure 3: Simulated and measured wind speeds from the periods 8:00-9:00 (a), 10:00-11:00 (b) and 12:00-13:00 (c) of the Høvsøre case. Profiles from simulations $H\phi_{const}$, $H\phi_t$ and $H\phi_{t+z}$ are represented by dotted, dashed and solid lines. The grey areas cover wind speeds measured by LIDAR and cup anemometers.

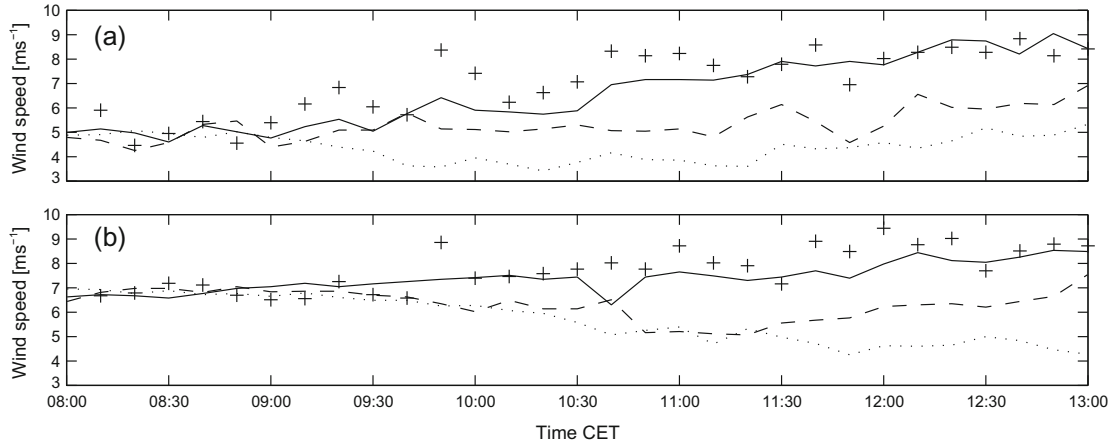

Figure 4: Time series of the wind speed at (a) 250 m and (b) 750 m from the Høvsøre case. LIDAR measurements are represented by crosses and simulated wind speed from $H\phi_{const}$, $H\phi_t$ and $H\phi_{t+z}$ by dotted, dashed and solid lines.

The chart shows an extensive area of uniform surface pressure surrounding the city of Hamburg. This is consistent with the weak pressure gradient and varying wind direction observed at the site. The mean direction of the wind at 10 m changes from 150° in the morning to 250° in the afternoon. With this change in wind direction, the area upstream of the site changes from light residential/rural to more industrial/urban (see Fig. 1).

The assumption of horizontal homogeneity is not as closely fulfilled as in the Høvsøre case. However, the urban/industrial sections of the upstream area consist mainly of low buildings on the order of 10 m and are less dense than the urban section north of the site. With a blending height of 1.5 to 5 times the mean obstacle height (CHRISTEN, 2005; BATCHVAROVA and GRYNING, 2006), we can assume that the individual buildings only influence the flow up to around 50 m. Detailed simulation of the urban roughness sublayer as described by e.g. LETZEL et al. (2008). (2008) and NAKAYAMA et al. (2012) is beyond the scope of this case study. We attempt to use one average roughness length for the entire upstream area.

The measured boundary layer height increased from a few hundred meters at 9:00 to 1500 m at 11:00 and 1800 m at 15:00. The relatively deep boundary layer means we have few LIDAR measurements above it. Thus, the driving pressure gradient cannot be estimated in the same way as in the Høvsøre case. Instead we use pressure measurements from the three ground-based sensors placed around the city of Hamburg, and wind speed measurements from three radio soundings performed during the studied period.

From the network of surface pressure measurements, we derive a pressure gradient across the city, which we assume drives the flow at the site. This type of surface measurement does, however, not reveal how the pressure gradient depends on height. To address this issue, we use data from radio soundings started at 9:30, 11:05 and 13:15 CET at the Hamburg site. As the sondes reach

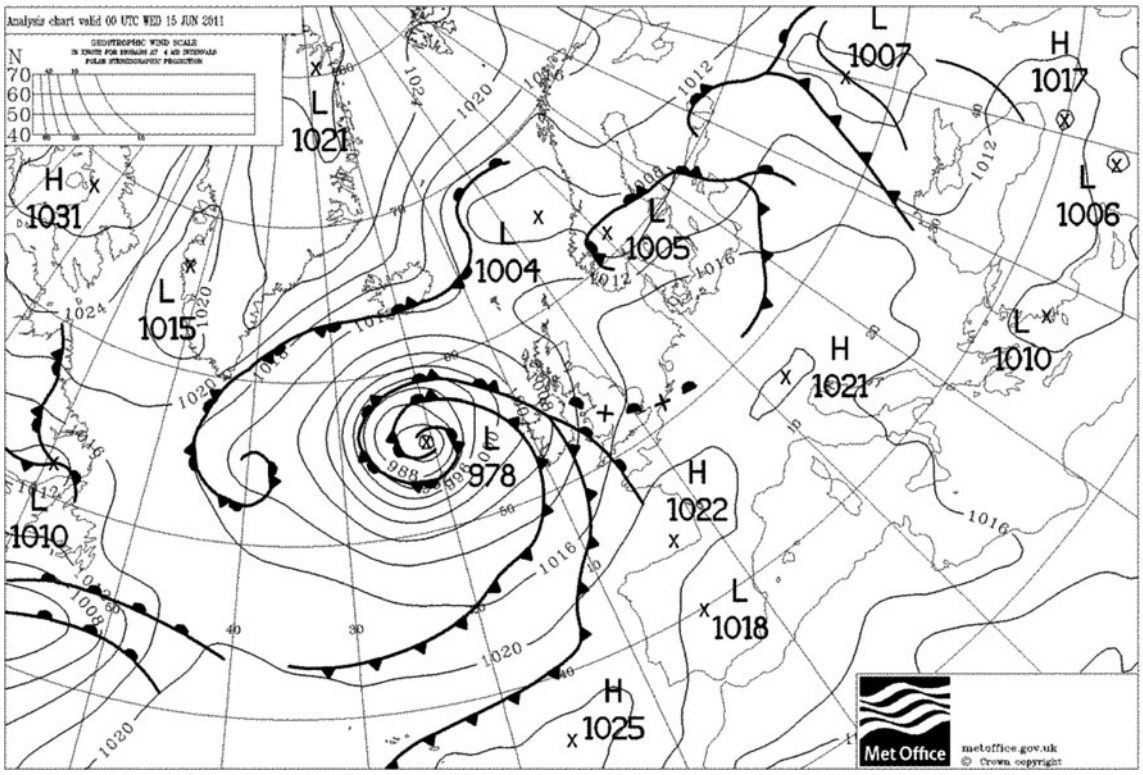

Figure 5: Met Office weather analysis chart valid at 01:00 CET on 15 June 2011 (Hamburg case study).

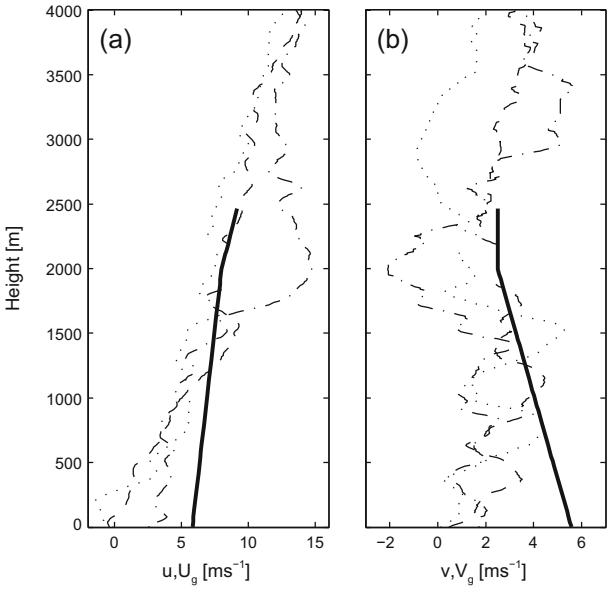

Figure 6: Initial profiles of U_g and V_g used in simulation Ha_{t+z} (solid lines), and profiles of u and v from radio soundings at 9:30, 11:05 and 13:15 (dotted, dash-dot and dashed lines).

above the ABL, they can in principle provide information about the pressure gradient in the same way as the LIDAR measurements in the Høvsøre case. The horizontal components of the wind speed inferred from the three radio soundings are shown in Fig. 6. Applying the same assumptions as in the Høvsøre case, and furthermore noting that the observed wind speed above 3000 m only changes little with time, we consider it to be effectively geostrophic (directly translatable to a pressure gradient) at these heights. Combining the information from the radio soundings and the surface pressure measurements, we estimate profiles of the pressure gradient for application in the LESs of the Hamburg case described in the following sections. LIDAR measurements from the Hamburg site are shown in Fig. 7 and 8.

4 The NCAR LES code and setup of simulations

The NCAR LES code is based on MOENG (1984) and SULLIVAN and PATTON (2011) and employs the subfilter scale model of SULLIVAN et al. (1994). It is pseudo spectral and surface inhomogeneities cannot be simulated.

The simulated flow is driven by a pressure gradient composed of $\left\langle \frac{\partial p}{\partial x} \right\rangle$ and $\left\langle \frac{\partial p}{\partial y} \right\rangle$. The angular brackets denote horizontal averages across the computational domain orientated with the x-axis in the west-east direction and the y-axis in the south-north direction. The pressure gradient is applied as an external forcing in terms of $U_g = -\frac{1}{f\rho}\left\langle \frac{\partial p}{\partial y} \right\rangle$ and $V_g = \frac{1}{f\rho}\left\langle \frac{\partial p}{\partial x} \right\rangle$, where f is the Coriolis-parameter and ρ is the air density. We will hereafter use this description of the pressure gradient. U_g and V_g can be specified as constant values or as functions of time t and/or height z.

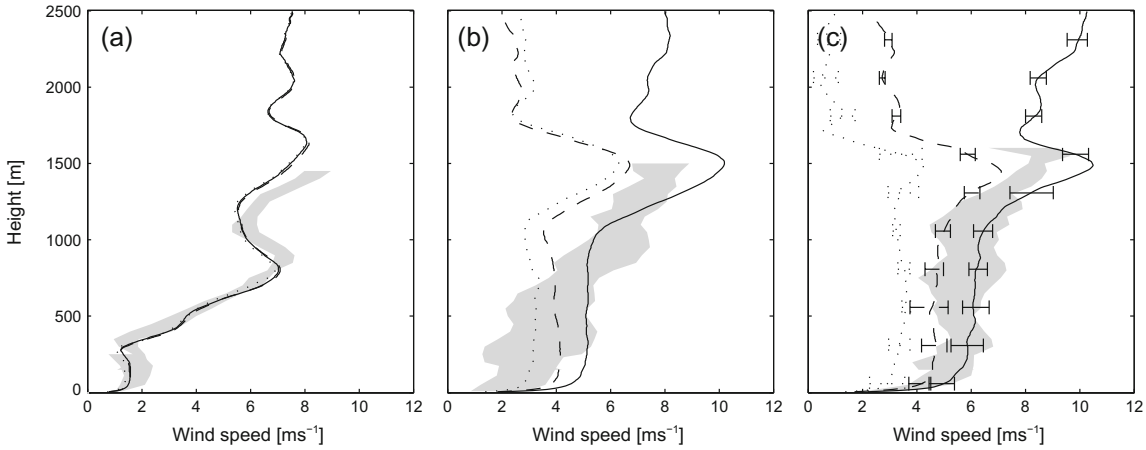

Figure 7: Simulated and measured wind speeds from the periods 9:00-10:00 (a), 12:30-13:30 (b) and 14:30-15:30 (c) of the Hamburg case. Profiles from simulations Ha_{const}, Ha_t, Ha_{t+z} are represented by dotted, dashed and solid lines. The grey areas cover wind speeds measured by LIDAR and sonic anemometers.

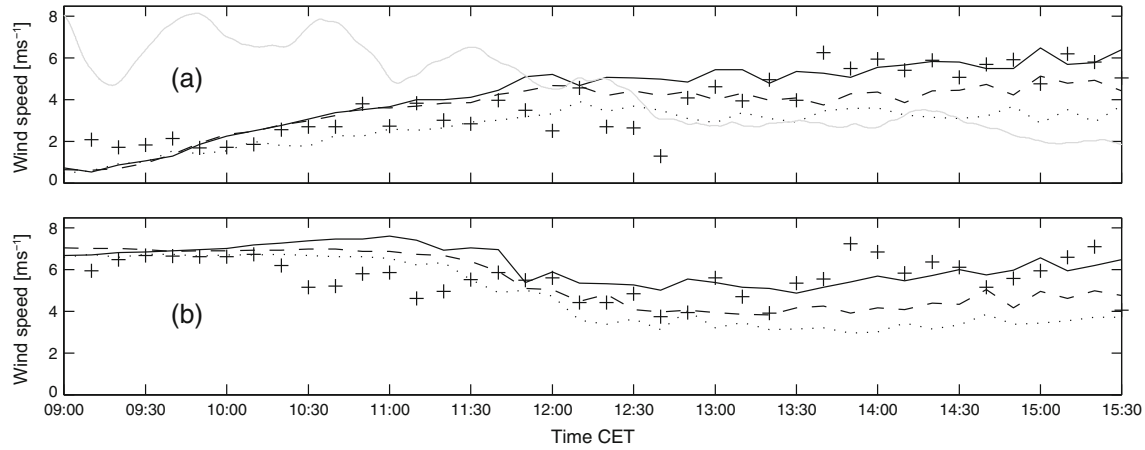

Figure 8: Time series of the wind speed at (a) 250 m and (b) 750 m from the Hamburg case. LIDAR measurements are represented by crosses and simulated wind speeds from Ha_{const}, Ha_t and Ha_{t+z} by dotted, dashed and solid black lines. The solid grey line in (a) marks the surface value of $(U_g^2 + V_g^2)^{1/2}$ applied in Ha_t and Ha_{t+z}.

A heat flux imposed at the lower boundary of the domain is used to calculate the surface value of the potential temperature through its value at the first grid level and Monin-Obukhov similarity.

The radiative boundary condition of KLEMP and DURRAN (1983) is used at the top of the computational domain. A third-order Runge-Kutta scheme is used for time stepping.

4.1 Setup of simulations

For each of the two sites, Høvsøre and Hamburg, we carry out three simulations with progressively more realistic assumptions for the driving pressure gradient. Table 1 provides an overview of all the simulations.

Each simulation is initialized with specified fields of the horizontal (west-east and south-north) and vertical velocity components u, v and w and the potential temperature θ. Random divergenceless small perturbations are added to the initial fields at grid points within 50 m of the surface to help initialize the turbulent motions. The process of going from the initially non-turbulent flow to a flow with quasi-steady turbulent fluxes is called spin-up (PATTON et al., 1998). In the Høvsøre and Hamburg case studies we find 0.5 and 1 hour of spin-up to be sufficient, based on the time it takes for the surface friction velocity to reach a quasi-steady state in simulations with constant forcing.

The observed humidity is in both cases generally low and the potential temperature is close to the virtual potential temperature. The influence of moisture on the wind speed is considered small and was not included in the simulations. However, intermittent appearance of clouds might have had effects which are neglected; for instance on the entrainment of air from above the ABL.

Table 1: Overview of Høvsøre (Hø) and Hamburg (Ha) simulations.

Simulation	Pressure gradient	Domain size	Grid points	Simulation period including spin-up
$Hø_{const}$	Constant	$6 \times 6 \times 2$ km^3	256^3	7:30 to 13:00
$Hø_t$	Function of t	$6 \times 6 \times 2$ km^3	256^3	7:30 to 13:00
$Hø_{t+z}$	Function of t and z	$6 \times 6 \times 2$ km^3	256^3	7:30 to 13:00
Ha_{const}	Constant	$7.5 \times 7.5 \times 2.5$ km^3	320^3	8:00 to 15:30
Ha_t	Function of t	$7.5 \times 7.5 \times 2.5$ km^3	320^3	8:00 to 15:30
Ha_{t+z}	Function of t and z	$7.5 \times 7.5 \times 2.5$ km^3	320^3	8:00 to 15:30

4.1.1 Høvsøre LES setup

All three Høvsøre simulations are performed in a domain of 6 km extent in the horizontal directions and 2 km in the vertical direction. This corresponds approximately to 6 and 2 times the expected maximum boundary layer height. The computational grid consists of 256 points in all three directions giving a vertical resolution of 8 m and a horizontal resolution of 23 m. The grid resolution test of SULLIVAN and PATTON (2011) suggests that this number of grid points is sufficiently high to get accurate results. It should however be noted that the simulated ABL of SULLIVAN and PATTON (2011) was more unstable than the one we study here, and the computational domain slightly smaller in the horizontal directions.

We apply a pressure gradient determined from observed wind speeds at altitudes above the boundary layer. From ceilometer backscatter measurements the ABL height is estimated to grow from 600 m in the morning to 900 m in the afternoon. Assuming the flow above the boundary layer is non-turbulent and horizontally homogenous, the averaged horizontal momentum equations can be reduced to:

$$\frac{\partial \langle u \rangle}{\partial t} = f\left(\langle v \rangle - V_g\right) \tag{1}$$

$$\frac{\partial \langle v \rangle}{\partial t} = f\left(U_g - \langle u \rangle\right).$$

In the $Hø_{const}$ simulation we furthermore assume the flow in the free atmosphere above the ABL to be stationary, i.e. $\frac{\partial \langle u \rangle}{\partial t} = \frac{\partial \langle v \rangle}{\partial t} = 0$, and we set:

$$U_g = \langle u \rangle_0 = -6\,\mathrm{ms}^{-1}$$

$$V_g = \langle v \rangle_0 = 0\,\mathrm{ms}^{-1}.$$

$\langle u \rangle_0$ and $\langle v \rangle_0$ represent the mean wind speed components around the time 8:30 corresponding to $t = 0$, where t is the simulation time minus one hour. All three Høvsøre simulations are in effect started at 7:30 to allow for a 0.5 hour spin-up period and for subsequent averaging over the period between 8:00 and 9:00. The used values for $\langle u \rangle_0$ and $\langle v \rangle_0$ are based on the observed mean wind speed above 600 m taken as an hourly average of the LIDAR measurements between 8:00 and 9:00 shown in Fig. 3 (a). The pressure gradient is in this simulation assumed to be constant with height representing barotropic conditions.

In general, however, the forces driving the flow of the ABL cannot be assumed to be stationary, and during the period studied here we do in fact also see variation of the observed mean wind speed above the ABL. More specifically, the u-component is observed to decrease from -6 ms^{-1} in the morning to -8 ms^{-1} in the afternoon (see Fig. 3 (a) and (c)). The v-component remains close to 0 ms^{-1}. In the $Hø_t$ and $Hø_{t+z}$ simulations we take this into account by assuming that above the ABL, $\langle u \rangle$ decreases linearly at a rate of $1.4 \cdot 10^{-4}$ ms^{-2} and $\langle v \rangle$ stays constant. Based on equation 1 this leads to:

$$U_g = \langle u \rangle_0 - 1.4 \cdot 10^{-4}\,\mathrm{ms}^{-2} \cdot t$$

$$V_g = \langle v \rangle_0 + 1.4 \cdot 10^{-4}\,\mathrm{ms}^{-2} \cdot f^{-1}.$$

In the $Hø_t$ simulation we assume barotropic conditions with U_g and V_g being constant with height, and as in the $Hø_{const}$ simulation we use $\langle u \rangle_0 = -6\,\mathrm{ms}^{-1}$ and $\langle v \rangle_0 = 0\,\mathrm{ms}^{-1}$.

In the $Hø_{t+z}$ simulation we assume baroclinic conditions with both U_g and V_g varying with height. The height variation is like the time variation estimated from the observed mean wind above the ABL. The estimated tendency above the ABL is extended to the surface and we use:

$$\langle u \rangle_0 = -8\,\mathrm{ms}^{-1} + z \cdot 0.002\,\mathrm{s}^{-1}$$

$$\langle v \rangle_0 = \begin{cases} 3\,\mathrm{ms}^{-1} - \mathrm{z} \cdot 0.003\,\mathrm{s}^{-1} & \text{for z} < 1000\,\mathrm{m} \\ 0\,\mathrm{ms}^{-1} & \text{for z} > 1000\,\mathrm{m} \end{cases}$$

The height dependence of U_g and V_g is kept constant during the simulation period in approximate agreement with LIDAR measurements. We do not show measured profiles of the individual wind speed components, but since the wind was mainly from the east and the direction only changed little with height, the height dependence of U_g can to a large extent be derived from the measurements of the wind speed shown in Fig. 3. The applied height dependence of V_g is most clearly seen from

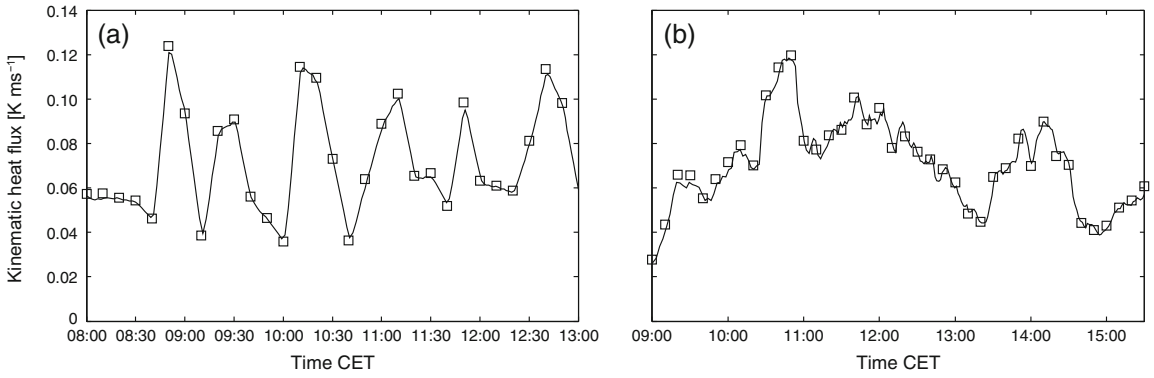

Figure 9: Kinematic heat flux measured at 10 m (squares) at the Høvsøre (a) and Hamburg (b) sites. The lines represent heat flux extracted from the lowest level of grid points in simulations $Hø_{t+z}$ (a) and Ha_{t+z} (b).

measurements between 8:00 and 9:00, but for simplicity we maintain it throughout the simulation.

In all three Høvsøre simulations we use an initial profile of the potential temperature given by:

$$\theta = \begin{cases} 280\,\mathrm{K} & \text{for } z < 550\,\mathrm{m} \\ 280\,\mathrm{K} + (z - 550\,\mathrm{m}) \cdot 0.025\,\mathrm{Km}^{-1} & \text{for } 550\,\mathrm{m} < z < 650\,\mathrm{m} \\ 282.5\,\mathrm{K} + (z - 650\,\mathrm{m}) \cdot 0.0034\,\mathrm{Km}^{-1} & \text{for } z > 650\,\mathrm{m} \end{cases}$$

We have no measurements of either temperature or pressure above 100 m, so the chosen profile is merely based on an assumption of a perfectly mixed layer up to 550 m capped by an inversion of 2.5 K between 550 and 650 m. Above the inversion we assume the potential temperature to decrease at 0.0034 Km^{-1} which is considered as a typical value in the free atmosphere.

The initial profiles of u and v are chosen such that the averaged profiles between 0.5 and 1.5 hours of simulation time match the observed wind speed components averaged between 8:00 and 9:00. At heights above the range of the LIDAR, the averaged profiles of u and v match the specified values of $\langle u \rangle_0$ and $\langle v \rangle_0$.

The heat flux applied at the lower boundary is set to follow the heat flux measured at 10 m which varies around 0.075 K m s^{-1} during the whole period as seen in Fig. 9. It is updated every time step using linear interpolation between measurements. The surface roughness length is set to 0.02 m (GRYNING et al., 2007) and the Coriolis parameter to $1.21 \cdot 10^{-4}$ s^{-1}.

4.1.2 Hamburg LES setup

For the Hamburg simulations, we use a computational domain of $7.5 \times 7.5 \times 2.5$ km^3 with 320 grid points in each direction. This gives the same resolution as in the Høvsøre simulations. A deeper boundary layer necessitates the bigger domain.

We apply a surface heat flux inferred from the measurements at 10 m shown in Fig. 9, and use a roughness length of 0.6 m (GRYNING et al., 2007). The Coriolis parameter is set to $1.16 \cdot 10^{-4}$ s^{-1}. As for the Høvsøre case, we perform three simulations with the applied pressure gradient being constant (Ha_{const}), time dependent (Ha_t) and time and height dependent (Ha_{t+z}).

In the Ha_{const} simulation we assume, that the pressure gradient is equal to its surface value at all heights, and keep it constant with time. It is specified to match the mean of the observed pressure gradient across the city between 9:00 and 15:30. This leads to U_g = 3.5 ms^{-1} and V_g = 2.4 ms^{-1}.

In the Ha_t simulation we keep the pressure gradient constant with height, but let it change with time as shown in Fig. 8 (a). It is updated every time step following the observed pressure gradient.

In the Ha_{t+z} simulation we assume baroclinic conditions. The pressure gradient is kept constant with time in the top part of the domain with U_g and V_g based on values of u and v from radio soundings started at 9:30, 11:05 and 13:15. We use observations from heights above 3000 m where the wind speed varies only little with time, and we can assume geostrophic balance. U_g is set to increase linearly from 8 ms^{-1} at 2000 m to 9.25 ms^{-1} at 2500. V_g is kept constant at 2.5 ms^{-1} in the same region. From 2000 m to the surface U_g and V_g are set to vary linearly to the time-varying values of the pressure gradient used in the Ha_t simulation. Fig. 6 shows wind speed components from the three radio soundings and the profiles of U_g and V_g at the beginning of simulation Ha_{t+z}.

The initial profiles of u, v and θ of the Hamburg LES runs are chosen, such that the profiles averaged between 1 and 2 hours of simulation time approximately match values from the radio sounding started at 9:30.

5 Results

In this section we present results of the LESs described in section 4 and compare them to measurements. The simulated wind speeds shown here are taken from a vertical column of grid points in the centre of the computational domain. As the measured wind speeds, they are averaged over 10 minute periods.

From the Høvsøre site we use cup anemometer measurements up to 100 m, and from the Hamburg site sonic anemometer measurements up to 250 m. We present wind LIDAR measurements up to heights between 900 and 1600 m. LIDAR measurements with data availability less than 70% are discarded.

5.1 Høvsøre results

Fig. 3 shows wind speeds from simulations $Hø_{const}$ (dotted lines), $Hø_t$ (dashed lines) and $Hø_{t+z}$ (solid lines) from the periods between 0.5 and 1.5, 2.5 and 3.5, and 4.5 and 5.5 hours of simulation time. The lines are 1-hour averaged profiles composed by six 10-minute profiles. The error bars in Fig. 3 (c) indicate the minimum and maximum 10-minute values at selected heights. These are left out in Fig. 3 (a) and (b) to give a more clear view of the mean profiles.

The grey areas cover the range of 10-minute averaged wind speeds measured by cup anemometers and LIDAR during the hours between 8:00 and 9:00, 10:00 and 11:00, and 12:00 and 13:00. We only show LIDAR measurements up to heights, where six 10-minute values are available per hour. The accuracy of wind speeds measured by LIDAR decreases with the Carrier to Noise ratio (CNR). Measurements with CNR higher than −30 dB are shown in dark grey, while measurements with CNR between −30 and −40 dB are shown in light grey. Cup anemometers provide the scalar wind speed. For consistency, we also present LIDAR measurements and LES wind speeds in terms of scalar averages. That is, averages over series of instantaneous or nearly instantaneous observations of the wind speed. This type of average differs from the vector average which consists of averaged values of the individual horizontal wind speed components (BROWER, 2012). In cases like this one, however, with only little variance in the wind direction the two types of averages will be quite close. Fig. 4 shows time series of measured and simulated wind speeds at heights of 250 and 750 m during the period between 8:00 and 13:00.

The $Hø_{const}$-simulation generally agrees poorly with measurements, and underestimates the wind speed by up to 4 ms^{-1} (~50%) after 5 hours of simulation time. The agreement is improved by the time-dependence of the pressure gradient included in the $Hø_t$ simulation. In particular, we see fair agreement between simulated and measured wind speeds above the ABL. This is, however, expected since the simulated wind speed in this region is almost directly proportional to the applied pressure gradient, which was determined from the observed wind. Within the ABL, the wind speed is still clearly underestimated.

The observed wind speed above the ABL decreases with height, as seen in Fig. 3 (a) above 600 m and in Fig. 3 (b) and (c) above 1000 m. Adding a height dependence to the pressure gradient, corresponding to what is observed, further improves the agreement between simulation ($Hø_{t+z}$) and measurements. In the period between 12:00 and 13:00 (Fig. 3 (c)) the agreement is good at nearly all heights. Before 11:00, too little vertical mixing and too slow of an increase of the pressure gradient seem to cause an underestimation of the wind speed in the ABL. This is indicated both by the shape of the simulated wind speed profile in Fig. 3 (b) and the time series of the wind speed at 250 m in Fig. 4 (a). The wind speed at 750 m (Fig. 4 (b)) from simulation $Hø_{t+z}$ follows the general trend of the measured wind speed, but with less variation. The surface friction velocity u_* is shown in Fig. 10, and it is in all three simulations within the scatter of the measured values.

The mean absolute error (MAE) and the root-mean-square error (RMSE) between the simulated data points in Fig. 4 and the equivalent measurements are given in Table 2. The MAE and RMSE are calculated as:

$$MAE = N^{-1} \sum_{i=1}^{N} |LIDAR_i - LES_i|$$

$$RMSE = \left(N^{-1} \sum_{i=1}^{N} (LIDAR_i - LES_i)^2 \right)^{0.5},$$

where N is the number of data points and $LIDAR_i$ and LES_i are wind speeds from the LIDAR and LES respectively.

5.2 Hamburg results

Fig. 7 shows wind speeds from simulations Ha_{const} (dotted lines), Ha_t (dashed lines) and Ha_{t+z} (solid lines) from the periods between 1 and 2, 4.5 and 5.5, and 6.5 and 7.5 hours of simulation time. As in Fig. 3, the lines are 1-hour averaged profiles composed by six 10-minute profiles. The grey areas cover wind speeds measured by sonic anemometers and LIDAR during the hours between 9:00 and 10:00, 12:30 and 13:30, and 14:30 and 15:30. The LIDAR measurements have a CNR above −30 dB.

In this case, the measured wind direction exhibits high variance due to the low wind speed and complex surroundings. Consequently we see a significant difference between scalar and vector averages of the measured wind speed. With this in mind, the following results are presented in terms of vector averages. Fig. 8 shows time series of measured and simulated wind speeds at heights of 250 and 750 m during the period between 9:00 and 15:30.

The results from the Hamburg case are not as clear as those from the Høvsøre case. The importance of including variations in time of the driving pressure gradient is, however, illustrated by the difference between the simulated profiles in Fig. 7 (c). The Ha_{const} simulation clearly underestimates the wind speed, while the profile from the Ha_t-simulation almost falls within the range measured profiles. Simulation Ha_{t+z} shows the best agreement with measurements in the period between 14:30 and 15:30, which suggests that baroclinity also

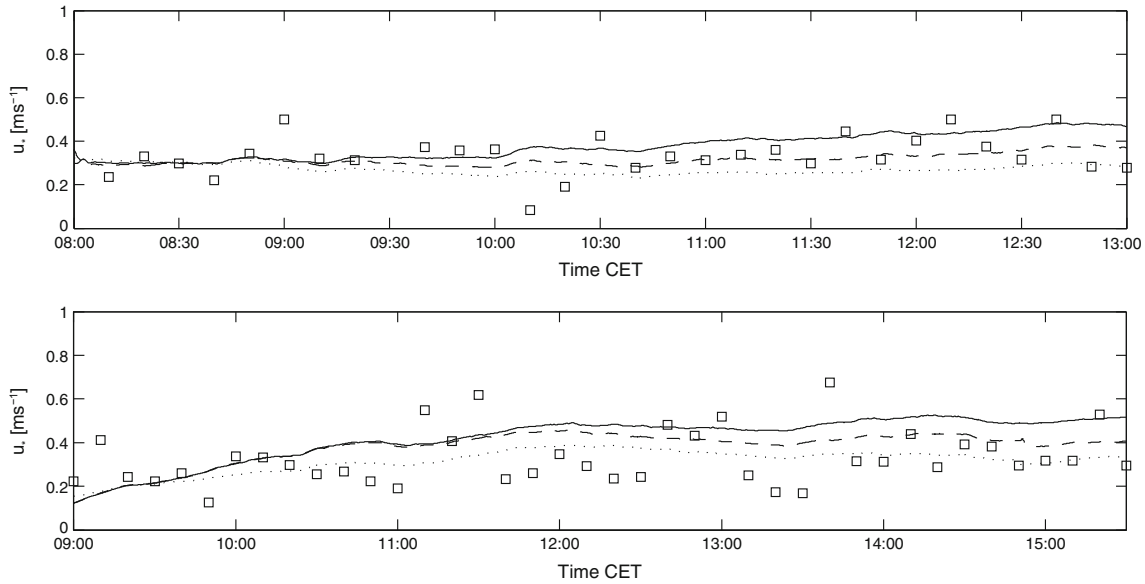

Figure 10: Time series of the measured and simulated friction velocities from the Høvsøre case (top) and Hamburg case (bottom). Tower measurements at 10 m are represented by squares and simulated values from $H\phi_{const}/Ha_{const}$, $H\phi_t/Ha_t$ and $H\phi_{t+z}$ /Ha_{t+z} at the grid levels closest to 10 m by dotted, dashed and solid black lines.

Table 2: Mean absolute errors and root-mean-square errors between LIDAR measurements and simulation results shown in Fig. 4 (Høvsøre case study).

	$H\phi_{const}$		$H\phi_t$		$H\phi_{t+z}$	
Height [m]	250	750	250	750	250	750
MAE [ms^{-1}]	2.8	2.2	1.8	1.5	0.7	0.6
RMSE [ms^{-1}]	3.1	2.7	2.1	1.9	0.8	0.7

Table 3: Mean absolute errors and root-mean-square errors between LIDAR measurements and simulation results shown in Fig. 8 (Hamburg case study).

	Ha_{const}		Ha_t		Ha_{t+z}	
Height [m]	250	750	250	750	250	750
MAE [ms^{-1}]	1.3	1.4	0.9	1.0	0.9	1.0
RMSE [ms^{-1}]	1.5	1.8	1.2	1.3	1.2	1.2

plays an important role in this case. However, as evident from both Fig. 7 (b) and Fig. 8 (a) and (b), the Ha_{t+z}-simulation generally overestimates the wind speed in the lowest part of the domain – especially between 11:00 and 13:30. Values of the MAE and the RMSE between the simulated data points in Fig. 8 and the equivalent measurements are shown in Table 3.

We suspect the specified vertical gradient of the forcing is too large near the surface. In fact we do not have any information about how the pressure gradient varies with height through the ABL. Assuming $\frac{\partial\left(\left\langle\frac{\partial p}{\partial x}\right\rangle,\left\langle\frac{\partial p}{\partial y}\right\rangle\right)}{\partial z}$ itself changes with height, measurements of either the horizontal temperature gradient or the horizontal pressure gradient as function of height are needed.

The surface friction velocity shown in Fig. 10 is in all three simulations quite close to the measured values, but especially in Ha_{t+z} somewhat overestimated.

5.3 Temperature effects

Fig. 11 shows measurements of potential temperature acquired by radiosondes started at 9:30, 11:05 and 13:15 from the Hamburg site and corresponding profiles from simulation Ha_{t+z}.

Due to the choice of initial conditions, the simulated temperature at 9:30 matches the radio sounding quite well, but at 11:05 the LES temperatures are too cold above the ABL (i.e. above 1500 m). Moreover, the ceilometer measurements show a decrease in the ABL height between 10:00 and 12:00 which points toward a lack of large scale subsidence in the LES. As described by e.g. Batchvarova and Gryning (1994) and Mirocha and Kosovic (2010) subsidence can reduce or even counteract the growth of the ABL.

During most of the period studied here, the tower-based temperature measurements show a faster increase than the simulated temperature even though the surface heat flux applied in the LES matches the measured heat flux, and compared to the radio sounding at 13:15 the simulated temperature is a few degrees too low throughout the ABL. This suggests advection of warm air, not included in the LES. Moreover, the vertical gradient of the simulated temperature above the ABL also agrees poorly with the radio sounding. The influence of the ABL height and the free atmosphere temperature gradient on the wind speed within the ABL is discussed in the

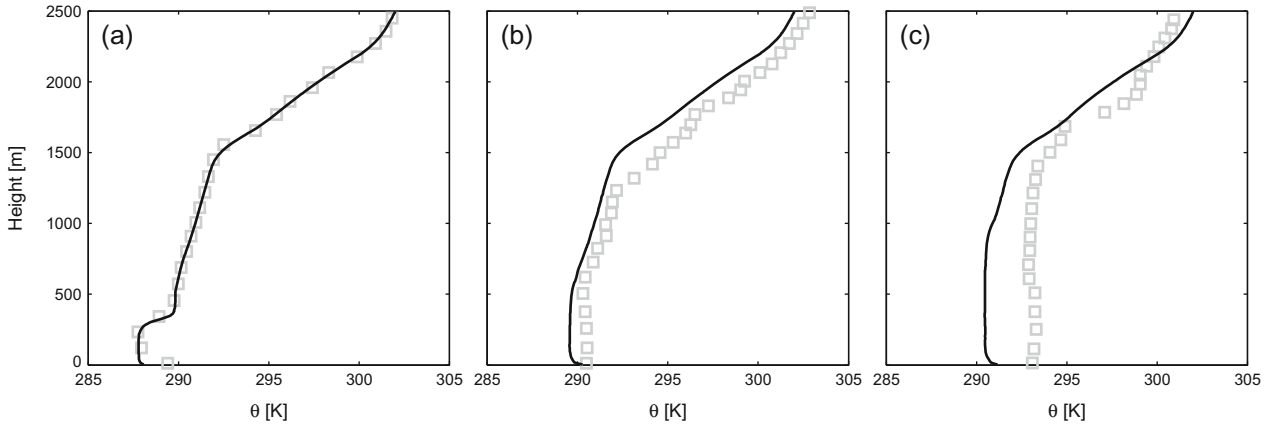

Figure 11: Potential temperature profiles from the Hamburg case. Markers represent radio soundings started at 9:30 (a), 11:05 (b) and 13:15 (c). The solid lines are ten-minute profiles from simulation Ha_{t+z} at corresponding times.

papers of GRYNING et al. (2007) and ZILITINKEVICH and ESAU (2005). However, the lengthy periods between the available radio soundings, and the apparently transient nature of the phenomena causing the observed temperature discrepancies, make them difficult to quantify and simulate.

In the Høvsøre case the simulated temperatures generally follow the tower-based measurements quite well. Unfortunately we have no measurements above 100 m in this case.

The height dependence of the driving pressure gradient is related to large-scale horizontal temperature gradients through the thermal wind equations. In simulations $Hø_{t+z}$ and Ha_{t+z}, the applied baroclinic shear corresponds to a horizontal temperature gradient on the order of 1×10^{-5} K m^{-1}, which is a typical value (ARYA and WYNGAARD, 1975). The associated advection of cold or warm air across the domain was not included in the simulations, since the effect on the simulated temperature would be small compared to e.g. the observed differences between the simulated temperature profiles and radio soundings in the Hamburg case.

6 Discussion

In the two case studies from Høvsøre and Hamburg we use LIDAR and radiosonde measurements, respectively, of the wind speed above the ABL to estimate the driving pressure gradient; in the Hamburg case as a supplement to ground-based measurements of the surface pressure gradient.

However, whereas the LIDAR provide measurements every 10 seconds from which a mean value over a longer period can be calculated, the radio soundings only provide nearly instantaneous measurements 1.5 and 2 hours apart. The mean ascent rates of the sondes are between 4 and 5 ms^{-1}, which means that the obtained wind profiles plotted in Fig. 6 essentially cover 800–1000 second periods. They can nevertheless not be considered as average profiles, since the sondes only spend an instant at each measuring height. Thus, the pressure gradient inferred from these in the Hamburg case is associated with higher uncertainty than that inferred from the averaged LIDAR profiles in the Høvsøre case.

An alternative approach to gain information about the pressure gradient for driving a realistic LES, is to use data from a mesoscale model such as WRF (SKAMAROCK et al., 2008). This approach is used by e.g. LUNDQUIST et al. (2010); TALBOT et al. (2012); RIZZA et al. (2013) and was considered for the Hamburg case study. However, since the surface pressure gradient derived from the pressure fields of the available WRF forecast fits poorly with the observed surface pressure gradient, we chose not to use the WRF pressure gradient.

7 Conclusion

At present, LES of the ABL is in most cases still confined to computational domains of only a few kilometers extent in each direction, with constant forcing. This means that phenomena acting on larger scales are not modelled. In the simulations presented here we account for such phenomena by including temporal and spatial variations of the external forcing applied in terms of a mean pressure gradient across the computational domain.

In two case studies from Høvsøre and Hamburg, we have estimated the pressure gradient from measurements of the wind speed above the ABL and from measurements of surface air pressure. At both sites we see variations in the pressure gradient with both time and height.

The effect on the wind speed of these variations is investigated by performing simulations with the forcing being constant ($Hø_{const}$ and Ha_{const}), time-dependent ($Hø_t$ and Ha_t) and both time- and height-dependent ($Hø_{t+z}$ and Ha_{t+z}).

In the Høvsøre case study we find that accurate specification of both height- and time-dependence of the

pressure gradient driving the flow is necessary to obtain good agreement between measured and simulated wind profiles.

In the Hamburg case, the effect of including the time dependence alone in the LES only improves the agreement between simulated and measured wind speeds towards the end of the simulation period. Including also the assumed height dependence generally improves the agreement above 1000 m, but causes an overestimation of the wind speed below. We take this as an indication that the vertical gradient of the pressure gradient within the ABL is not constant with height, but decreases near the surface. However, it must be concluded that the measurements available in this case study are not sufficient to accurately estimate the effective baroclinicity.

In the Hamburg case, we furthermore see differences between measured and simulated profiles of potential temperature, caused by large scale subsidence and advection not accounted for in the LES. More frequent radio soundings would help us to include such phenomena and study their influence on the wind speed.

With increasing computer power LES of realistic atmospheric flows is likely to become more common in the future with applications including assessment of wind resources and turbulence characteristics at potential sites for energy production (EMEIS, 2012) and prediction of pollutant dispersion in cities. As the work presented here illustrates, careful treatment of spatially and temporally varying forcing can be essential for obtaining accurate results.

Acknowledgments

The study was supported by the Danish Council for Strategic Research, project number 2104-08-0025 named "Tall Wind". We would like to thank the Test and Measurements section of DTU Wind Energy for the maintenance of the Høvsøre database.

References

ARYA S.P., 2001: Introduction to micrometeorology. – Academic Press, San Diego, 420 pp.

ARYA, S.P.S., J.C. WYNGAARD, 1975: Effect of baroclinicity on wind profiles and the geostrophic drag law for the convective planetary boundary layer. – J. Atmos. Sci. **32**, 767–778.

BASU, S., J.-F. VINUESA, A. SWIFT, 2008: Dynamic LES modeling of a diurnal cycle. – J. Appl. Meteor. Climatol. **47**, 1156–1174.

BATCHVAROVA, E., S.-E. GRYNING, 1994: An applied model for the height of the daytime mixed layer and the entrainment zone. – Bound.-Layer Meteor. **71**, 311–323.

BATCHVAROVA, E., S.-E. GRYNING, 2006: Progress in urban dispersion studies. – Theor. Appl. Climatol. **84**, 57–67.

BEARE, R.J., M.K. MACVEAN, A.A.M. HOLTSLAG, J. CUXART, I. ESAU, J.-C. GOLAZ, M.A. JIMENEZ, M. KHAIROUTDINOV, B. KOSOVIC, D. LEWELLEN, T.S. LUND, J.K. LUNDQUIST, A. MCCABE, A.F. MOENE, Y. NOH, S. RAASCH, P. SULLIVAN, 2006: An intercomparison of large-eddy simulations of the stable boundary layer. – Bound.-Layer Meteor. **118**, 247–272.

BROWER M.C., 2012: Wind Resource Assessment: A Practical Guide to Developing a Wind Project. – Wiley, 296 pp.

BRÜMMER, B., I. LANGE, H. KONOW, 2012: Atmospheric boundary layer measurements at the 280 m high Hamburg weather mast 1995–2011: mean annual and diurnal cycles. – Meteorol. Z. **21**, 319–335.

CHRISTEN A., 2005: Atmospheric turbulence and surface energy exchange in urban enviroments – Results from the Basel Urban Boundary Layer Experiment (BUBBLE). – University of Basel, 140 pp.

CLARKE R.H., R.R. BROOK, D.G. REID, A.J. TROUP, 1971: The Wangara experiment: Boundary layer data. – C.S.I.R.O., Melbourne.

DEARDORFF, J.W., 1970: Preliminary results from numerical integrations of the unstable planetary boundary layer. – J. Atmos. Sci. **27**, 1209–1211.

———, 1972: Numerical investigation of neutral and unstable planetary boundary layers. – J. Atmos. Sci. **29**, 91–115.

———, 1974: Three–dimensional numerical Study of the height and mean structure of a heated planetary boundary layer. – Bound.-Layer Meteor. **7**, 81–106.

EMEIS S., 2012: Wind energy meteorology. – Springer-Verlag Berlin Heidelberg, Berlin, 196 pp.

FLOORS, R., C.L. VINCENT, S.-E. GRYNING, A. PEÑA, E. BATCHVAROVA, 2013: The wind profile in the coastal boundary layer: Wind lidar measurements and numerical modelling. – Bound.-Layer Meteor. **147**, 469–491.

GRYNING, S.E., E. BATCHVAROVA, B. BRÜMMER, H. JØRGENSEN, S. LARSEN, 2007: On the extension of the wind profile over homogeneous terrain beyond the surface boundary layer. – Bound.-Layer Meteor. **124**, 251–268.

KELLY, M., S.-E. GRYNING, 2010: Long-term mean wind profiles based on similarity theory. – Bound.-Layer Meteor. **136**, 377–390.

KLEMP, J.B., D.R. DURRAN, 1983: An upper boundary condition permitting internal gravity wave radiation in numerical mesoscale models. – Mon. Wea. Rev. **111**, 430–444.

KOSOVIC, B., J.A. CURRY, 2000: A large eddy simulation study of a quasi-steady, stably stratified atmospheric boundary layer. – J. Atmos. Sci. **57**, 1052–1068.

KUMAR, V., G. SVENSSON, A.A.M. HOLTSLAG, C. MENEVEAU, M.B. PARLANGE, 2010: Impact of surface flux formulations and geostrophic forcing on large-eddy simulations of diurnal atmospheric boundary layer flow. – J. Appl. Meteor. Climatol. **49**, 1496–1516.

LETZEL, M.O., M. KRANE, S. RAASCH, 2008: High resolution urban large-eddy simulation studies from street canyon to neighbourhood scale. – Atmos. Environ. **42**, 8770–8784.

LUNDQUIST J.K., J.D. MIROCHA, B. KOSOVIC, 2010: Nesting large-eddy simulations within mesoscale simulations

in WRF for wind energy applications. – Proceedings of the Fifth International Symposium on Computational Wind Engineering, Chapel Hill, NC, May 23–27.

MIKKELSEN T., 2009: On mean wind and turbulence profile measurements from ground-based wind lidars: limitations in time and space resolution with continuous wave and pulsed lidar systems. European Wind Energy Conference and Exhibition, Marseille, FR, March 16–19.

MIROCHA, J.D., B. KOSOVIC, 2010: A large-eddy simulation study of the influence of subsidence on the stably stratified atmospheric boundary layer. – Bound.-Layer Meteor. **134**, 1–21.

MOENG, C.-H., 1984: A Large–eddy–simulation model for the study of planetary boundary–layer turbulence. – J. Atmos. Sci. **41**, 2052–2062.

MOENG, C.-H., P.P. SULLIVAN, 1994: A comparison of shear– and buoyancy–driven planetary boundary layer flows. – J. Atmos. Sci. **51**, 999–1022.

NAKAYAMA, H., T. TAKEMI, H. NAGAI, 2012: Large–eddy simulation of urban boundary–layer flows by generating turbulent inflows from mesoscale meteorological simulations. – Atmos. Sci. Lett. **13**, 180–186.

PATTON, E.G., R.H. SHAW, M.J. JUDD, M.R. RAUPACH, 1998: Large–eddy simulation of windbreak flow. – Bound.-Layer Meteor. **87**, 275–306.

RIZZA, U., M.M. MIGLIETTA, O.C. ACEVEDO, V. ANABOR, G.A. DEGRAZIA, A.G. GOULART, H.R. ZIMMERMAN, 2013: Large-eddy simulation of the planetary boundary layer under baroclinic conditions during daytime and sunset turbulence. – Meteorol. Appl. **20**, 56–71.

SCHMIDT, H., U. SCHUMANN, 1989: Coherent structure of the convective boundary layer derived from large–eddy simulations. – J. Fluid Mech. **200**, 511–562.

SKAMAROCK W., J.B. KLEMP, J. DUDHIA, D.O. GILL, D.M. BARKER, M.G. DUDA, X.-Y. HUANG, W. WANG, 2008: A Description of the Advanced Research WRF Version 3. – University Corporation for Atmospheric Research, Boulder, 113 pp.

SULLIVAN, P.P., E.G. PATTON, 2011: The effect of mesh resolution on convective boundary layer statistics and structures generated by large–eddy simulation. – J. Atmos. Sci. **68**, 2395–2415.

SULLIVAN, P.P., J.C. MCWILLIAMS, C.-H. MOENG, 1994: A subgrid–scale model for large–eddy simulation of planetary boundary–layer flows. – Bound.-Layer Meteor. **71**, 247–276.

SULLIVAN, P.P., C.-H. MOENG, B. STEVENS, D.H. LENSCHOW, S.D. MAYOR, 1998: Structure of the entrainment zone capping the convective atmospheric boundary layer. – J. Atmos. Sci. **55**, 3042–3064.

TALBOT, C., E. BOU-ZEID, J. SMITH, 2012: Nested mesoscale large–eddy simulations with WRF: Performance in real test cases. – J. Hydrometeor. **13**, 1421–1441.

ZILITINKEVICH, S.S., I.N. ESAU, 2005: Resistance and heat-transfer laws for stable and neutral planetary boundary layers: Old theory advanced and re-evaluated. – Quart. J. Roy. Meteor. Soc. **131**, 1863–1892.